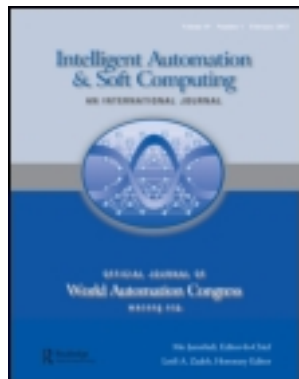


This article was downloaded by: [National Chiao Tung University 國立交通大學]

On: 25 April 2014, At: 02:08

Publisher: Taylor & Francis

Informa Ltd Registered in England and Wales Registered Number: 1072954 Registered office: Mortimer House, 37-41 Mortimer Street, London W1T 3JH, UK



## Intelligent Automation & Soft Computing

Publication details, including instructions for authors and subscription information:

<http://www.tandfonline.com/loi/tasj20>

### The Chemical Stain Inspection of Polysilicon Solar Cell Wafer by the Fuzzy Theory Method

Chern-Sheng Lin <sup>a</sup>, Chih-Wei Lin <sup>b</sup>, Shih-Wei Yang <sup>c</sup>, Shir-Kuan Lin <sup>c</sup> & Chuang-Chien Chiu <sup>a</sup>

<sup>a</sup> Department of Automatic Control Engineering, Feng Chia University, Taichung, Taiwan

<sup>b</sup> Wonder System Corp., Taichung, Taiwan

<sup>c</sup> Institute of Electrical and Control Engineering, National Chiao Tung University, Hsinchu, Taiwan

Published online: 25 Mar 2013.

To cite this article: Chern-Sheng Lin, Chih-Wei Lin, Shih-Wei Yang, Shir-Kuan Lin & Chuang-Chien Chiu (2013) The Chemical Stain Inspection of Polysilicon Solar Cell Wafer by the Fuzzy Theory Method, Intelligent Automation & Soft Computing, 19:3, 391-406, DOI: [10.1080/10798587.2013.778052](https://doi.org/10.1080/10798587.2013.778052)

To link to this article: <http://dx.doi.org/10.1080/10798587.2013.778052>

PLEASE SCROLL DOWN FOR ARTICLE

Taylor & Francis makes every effort to ensure the accuracy of all the information (the "Content") contained in the publications on our platform. However, Taylor & Francis, our agents, and our licensors make no representations or warranties whatsoever as to the accuracy, completeness, or suitability for any purpose of the Content. Any opinions and views expressed in this publication are the opinions and views of the authors, and are not the views of or endorsed by Taylor & Francis. The accuracy of the Content should not be relied upon and should be independently verified with primary sources of information. Taylor and Francis shall not be liable for any losses, actions, claims, proceedings, demands, costs, expenses, damages, and other liabilities whatsoever or howsoever caused arising directly or indirectly in connection with, in relation to or arising out of the use of the Content.

This article may be used for research, teaching, and private study purposes. Any substantial or systematic reproduction, redistribution, reselling, loan, sub-licensing, systematic supply, or distribution in any form to anyone is expressly forbidden. Terms & Conditions of access and use can be found at <http://www.tandfonline.com/page/terms-and-conditions>



## THE CHEMICAL STAIN INSPECTION OF POLYSILICON SOLAR CELL WAFER BY THE FUZZY THEORY METHOD

**CHERN-SHENG LIN\***

*Department of Automatic Control Engineering, Feng Chia University, Taichung, Taiwan*

**CHIH-WEI LIN**

*Wonder System Corp., Taichung, Taiwan*

**SHIH-WEI YANG AND SHIR-KUAN LIN**

*Institute of Electrical and Control Engineering, National Chiao Tung University, Hsinchu, Taiwan*

AND

**CHUANG-CHIEN CHIU**

*Department of Automatic Control Engineering, Feng Chia University, Taichung, Taiwan*

**ABSTRACT**—This study proposed an automatic optical inspection (AOI) technique to improve the inspection of chemical stains on solar wafers. Poly-silicon solar cell wafers were inspected for chemical stains, and the inspection was rapid and stable. The system used a laser-reflection-point-based AOI method for solar wafer chemical stain inspection. Based on the fuzzy theory, the image binarization algorithm could efficiently filter irrelevant image information, and the back-propagation method was also utilized to determine if the image was stained. The inspection algorithm integrated fuzzy theory and the back-propagation method in order to shorten the comparison time and quickly find the target. The experiment proved that the validity of the proposed method could achieve a recognition rate of 98% from among 1000 images.

**Key Words:** Solar wafer; Laser-reflection-point based AOI method; Chemical stain inspection; Fuzzy theory; Back-propagation; Image binarization algorithm; Stain recognition

### 1. INTRODUCTION

Solar energy has the potential to fulfill a major part of the sustainable energy demands of future generations. According to different materials, solar cells can be roughly divided into [1]: 1) single-crystalline silicon solar cells; 2) poly-crystalline silicon solar cells; 3) multi-material cells using inorganic salts such as gallium arsenide III-V compounds, cadmium sulfide, copper indium selenium compounds; and 4) amorphous thin film solar cells etc.

Solar cell polysilicon material consists of many monocrystals of various sizes, and its atomic arrangement is not periodic. It is usually made by casting and solidifying fused silicon; hence, the cost is

---

\*Corresponding author. Email: [lincs@fcu.edu.tw](mailto:lincs@fcu.edu.tw)

low, and the output of polysilicon-based solar cells has gradually exceeded that of monocrystal-silicon-based solar cells. Amorphous silicon based substances include GaAs, GaInP, InGaAs, CdTe, CuInSe<sub>2</sub> (CIS), and CuInGaSe<sub>2</sub>(CIGS), and the derived solar cells have high efficiencies. Although there are many solar panel inspection methods available, fragile or scratch-prone materials, such as solar panels, are unsuitable for probe inspection; hence, the automatic optical inspection (AOI) system is widely applied. During solar cell production, surface stains derived from various chemical processes have a serious impact on product quality. However, there are defects in the production lines that traditional AOI systems fail to inspect. For example, surface chemical contaminations have a great impact on solar panels; however, the accuracy rate of such inspections is low. When using a traditional AOI system to analyze surface chemical contamination, the accuracy rate is only 30–50%; hence, methods that improve the accuracy rate of auto-inspections have become a pressing topic.

Poly-crystalline silicon solar cells are made from high-quality silicon with a thickness of 180 ~ 350  $\mu\text{m}$ . Such silicon wafers are cut from Czochralski or casted silicon ingots [2]. The wafers are usually lightly p-type doped. To make a solar cell from the wafer, a surface diffusion of n-type dopants is performed on the front side of the wafer. This forms a p-n junction a few hundred nanometers below the surface [3]. Antireflection coatings, which increase the amount of light coupled into the solar cell [4], are typically next applied. Over the past decade, silicon nitride has gradually replaced titanium dioxide as the antireflection coating of choice, because of its excellent surface passivation qualities. It is typically applied in a layer several hundred nanometers thick using plasma-enhanced chemical vapor deposition (PECVD). In recent years solar cells have had textured front surfaces [5] that, like antireflection coatings, serve to increase the amount of light coupled into the cell.

The wafer has a full area metal contact on the back surface, and a grid-like metal contact made up of fine fingers and larger busbars is screen-printed onto the front surface using a silver paste. The rear contact is also formed by screen-printing a metal paste, typically aluminum. Usually this contact covers the entire rear side of the cell, although in some cell designs it is printed in a grid pattern [6]. The paste is then fired at several hundred degrees Celsius to form metal electrodes that are in ohmic contact with the silicon. After the metal contacts are made, the solar cells are interconnected in series/parallel by flat wires or metal ribbons, and are then assembled into modules or solar panels. Figure 1(a) illustrates a poly-crystalline silicon solar cell process.

However, during the manufacturing process of the solar cell, several kinds of defects may occur, such as residual acid, water stains, saw marks, busbar peeling, and so on. If these defects are ignored, there will be cost concerns, and the inferior wafers will impact the production efficiency [7,8,9]. Increasing methods for detecting defects in solar cells, strings and modules have been proposed. Belyaev et al. [10] presented a resonance vibration approach to measure the residual stress in the poly-crystalline silicon wafers used in solar cell manufacturing. This method can detect cracks as small as 5–10  $\mu\text{m}$ ; however, the wafer has to be submerged in a water bath. Li et al. [11] developed a hyperspectral imaging system to identify cracks and fracture defects in solar cells using the spectral angle mapper algorithm. Hilmersson et al. [12] used an impact test method to detect the cracks in single-crystalline silicon wafers, which, according to the data from defective wafers with lower natural frequencies, higher damping levels, and lower peak amplitudes. Tsai et al. [13] proposed a machine vision scheme for detecting micro-crack defects in solar wafer manufacturing. The proposed diffusion model takes both gray-level and gradients as features to adjust the diffusion coefficients. Only the pixels with both low gray-levels and high gradients will generate high diffusion coefficients. It then smooths the suspected defect region and preserves the original gray-levels of the faultless background. By subtracting the diffused image from the original image, the micro-crack can be distinctly enhanced in the difference image. Zhang et al. [14] presented a four-layer feed forward fuzzy neural network with an associated learning algorithm. The FNN combines the advantages of fuzzy logic systems and neural

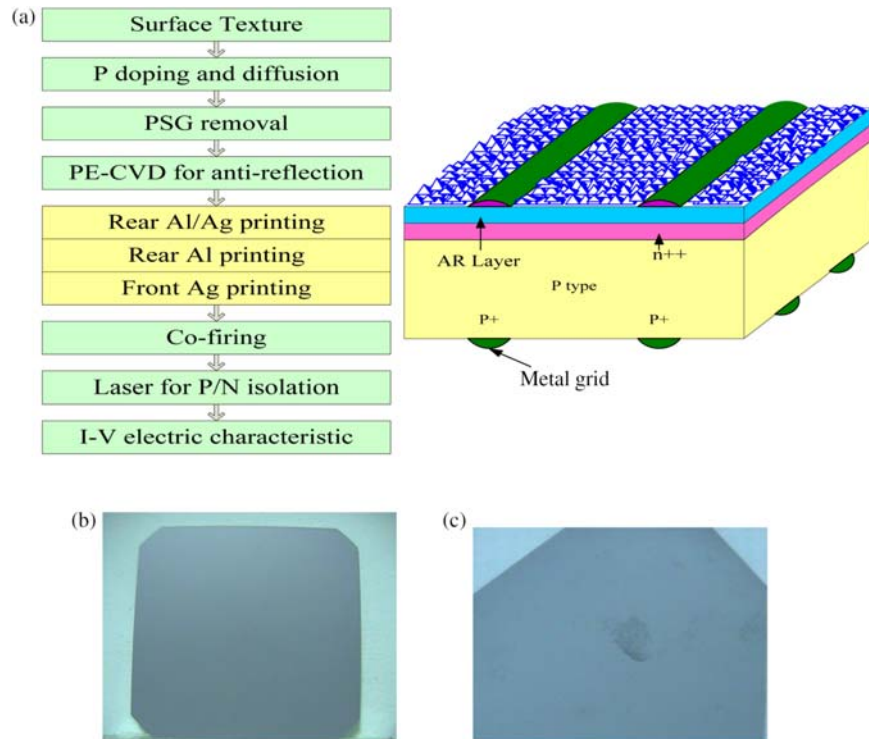


Figure 1. (a) A poly-crystalline silicon solar cell process; (b) Polysilicon solar cell wafer (not stained); (c) Polysilicon solar cell wafer (stained).

networks, providing a convenient method for solving complex recognition processes such as TFT-LCD mura evaluations.

Numerous applications of defect inspection using fuzzy neural networks have been developed [14–15], but they have mainly been used on TFT-LCD (thin film transistor liquid crystal display). Unlike the ripe techniques of TFT-LCD, methods that use a fuzzy neural network for detecting defects on solar cells have been discussed less. In this paper, a novel method of inspecting defects in the chemical process of poly-crystalline solar cell wafers by the fuzzy theory was presented. Laser-reflected spots of quality solar wafers were used as a standard reference for comparison with the spots of inferior wafers. In addition, the fuzzy algorithm and back-propagation method were applied in the system in order to improve the system's efficiency.

## 2. BACK-PROPAGATION METHOD

This study analyzed solar wafer images based on laser reflection points and designed a chemical stain analysis program to identify whether a light reflection point on a solar wafer was a chemical stain. This program included image-processing techniques such as fuzzy inference binarization, image feature acquisition, and back-propagation recognition. During the experiments, a He-Ne laser beam was projected onto a solar wafer, via two reflectors, and then reflected onto a screen to produce a laser reflection point. When the laser reflection point was formed on the screen, a computer captured this image with a digital

camera (CCD) and conducted subsequent analysis. If the projection site on the solar wafer had no chemical stains, the resulted light reflection point image would be a quasi-circular and luminous image; contrarily, if the projection site on the solar wafer had chemical stains, the resulting light reflection point image would have an irregular geometric figure.

Upon acquiring an image, it must first be binarized in order to filter out irrelevant information. During binarization, noises often occur on an image; hence, other image processing techniques are required to filter the image. In this study, fuzzy inference was used to binarize an image to filter out noises and highlight image features.

The back-propagation learning algorithm [15–16] in this study utilized a supervised learning algorithm, which conducts its computed learning processes in batches. The eigenvalue of each laser reflection point image is entered into the network in order to calculate the output, and the expected output is set for each data entry and represents whether there is contamination. Network errors are equal to the expected value minus the output; such errors propagate from the back-end to the front-end in order to modify network parameters and achieve network convergence.

Suppose that, during batch-training of the laser reflection point feature images, the eigenvector of each laser reflection point is  $X$  and each target output vector is  $T$ . In the back-propagation neural network (BPNN), the input of the  $j^{\text{th}}$  neuron in the  $n^{\text{th}}$  layer will be  $X_j^n$ , and the output of the  $j^{\text{th}}$  neuron in the  $n^{\text{th}}$  layer will be  $Y_j^n$ ; thus, the expected output of the  $j^{\text{th}}$  neuron in the output layer is  $T_j$ . The interconnecting weight between the  $i^{\text{th}}$  neuron and the  $j^{\text{th}}$  neuron is  $W_{ij}$ , and the threshold of the  $j^{\text{th}}$  neuron is  $\theta_j$ . When  $f(x)$  denotes the network activation function, the sigmoid function,  $1/1 + e^{-x}$  is adopted. Eq. (1) represents the network neuron output in the  $n^{\text{th}}$  layer:

$$Y_j^n = f(\text{net}_j^{n-1}) = f\left(\sum_i W_{ij} \times X_i - \theta_j\right) \quad (1)$$

The general BPNN error function is expressed by Eq. (2). The error is the difference between the target output and the expected output, which is expected to decrease through learning [17]:

$$E = \frac{\sum (T_j - Y_j)^2}{2} \quad (2)$$

Adjusting the network neuron weight ( $W$ ) and the neuron threshold ( $\theta$ ) can decrease errors between the output and the expected value. The main purpose of a neural network learning algorithm is to adjust the interconnecting weight and the neuron threshold. The weight correction formula is as shown in Eq. (3), in which  $\Delta W$  is the corrected value of the interconnecting weight:

$$W = W + \Delta W \quad (3)$$

Next, take a partial derivative, with respect to the interconnecting weight and neuron threshold from the output layer to the hidden layer. The results are shown in Eq. (4) and (5).

$$\Delta W_{ij} = -\eta \times [-(T_j - Y_j)] \times f'(\text{net}_j) \times Y_{hj} = \eta \times (T_j - Y_j) \times (1 - Y_j) \times Y_j \times Y_{hj} = \eta \times s_y \times Y_h \quad (4)$$

$$\begin{aligned} \Delta \theta_j &= -\eta \frac{\partial}{\partial Y_o} \left[ \frac{1}{2} \sum_k (T_k - Y_k)^2 \right] \times \frac{\partial}{\partial \text{net}} [f(\text{net})] \times \frac{\partial}{\partial \theta_j} \left[ \sum_k W_{ik} \times Y_h - \theta_j \right] \\ &= -\eta \times (T_j - Y_o) \times \left( 1 - \frac{1}{1 + e^{-\text{net}}} \right) \times \left( \frac{1}{1 + e^{-\text{net}}} \right) = -\eta \times s_y \end{aligned} \quad (5)$$

where,  $\Delta W_{ij}$  denotes the corrected value of the interconnecting weight between the  $i^{th}$  neuron in the hidden layer and the  $j^{th}$  neuron in the output layer,  $\Delta \theta_j$  denotes the corrected threshold value of the  $j^{th}$  neuron in the output layer,  $Y_{hj}$  denotes the output of the  $j^{th}$  neuron in the hidden layer,  $\eta$  denotes the inertial factor learning rate, which normally ranges between  $0 \sim 1$ , and  $s_y = (T_j - Y_j) \times f'(net_j)$  denotes the error of the output layer.

For the hidden and input layers, the interconnecting weight and neuron threshold correction formula is as follows:

$$\Delta W_{ij} = -\eta \times \left[ \sum_k \frac{\partial E}{\partial net_k^{n+1}} \times \frac{\partial net_k^{n+1}}{\partial Y_j} \right] \times \frac{\partial Y_j}{\partial net_j} \times \frac{\partial net_j}{\partial W_{ij}} = -\eta \times \sum_k (-s_k^n \times W_{jk}) \times f'(net) \times y_{hj} \quad (6)$$

Similarly, the hidden layer neuron threshold correction formula can be deduced:

$$\begin{aligned} \Delta \theta_h &= -\eta \frac{\partial E}{\partial \theta_h} = -\eta \frac{\partial E}{\partial Y_j^n} \times \frac{\partial Y_j^n}{\partial net_j^n} \times \frac{\partial net_j^n}{\partial \theta_h} = -\eta \times \left[ \sum_k \frac{\partial E}{\partial net_k^{n+1}} \times \frac{\partial net_k^{n+1}}{\partial Y_j} \times \frac{\partial Y_j}{\partial net_j} \times \frac{\partial net_j}{\partial \theta_h} \right] \\ &= -\eta \times \sum_k (s_k^n \times W_{jk}) \times f'(net) \end{aligned} \quad (7)$$

The modified neuron interconnecting weight and threshold are as follows:

$$W_{ij} = W_{ij} + \Delta W_{ij} = W_{ij} + \eta \times s \times Y_h \quad (8)$$

$$\theta_j = \theta_j + \Delta \theta_j = \theta_j - \eta \times s \quad (9)$$

To determine if back-propagation learning is sufficient to recognize contaminations, the root mean square (RMS) is normally used to determine if the network convergence is decreasing. When the network finishes one learning cycle, the value of the network RMS is checked to ensure that it is less than the preset error. Eq. (10) shows the network RMS formula:

$$RMS = \sqrt{\frac{\sum_p^M \sum_j^N (T_j^p - Y_j^p)^2}{M \times N}} \quad (10)$$

where,  $M$  denotes the number of training laser reflection point images,  $N$  denotes the number of output layer neurons in a neural network,  $T_j^p$  denotes the target output of the  $j^{th}$  neuron in the example of the  $p^{th}$  laser reflection point image, and  $Y_j^p$  denotes the inferred output of the  $j^{th}$  neuron in the example of the  $p^{th}$  laser reflection point image.

The target of this study was polysilicon solar cell wafers. The tested image of a solar cell panel is shown in Figure 1(b) and (c). The laser reflection point images were acquired using CCD for subsequent analysis. The image resolution was  $640 \times 480$ , and the image format was RGB. This study adopted a fuzzy theory-derived image processing algorithm. After the images were loaded, binarization was performed in order to filter out irrelevant information. During image binarization, noises often occur in the images; thus, other image processing techniques are required in order to filter images prior to

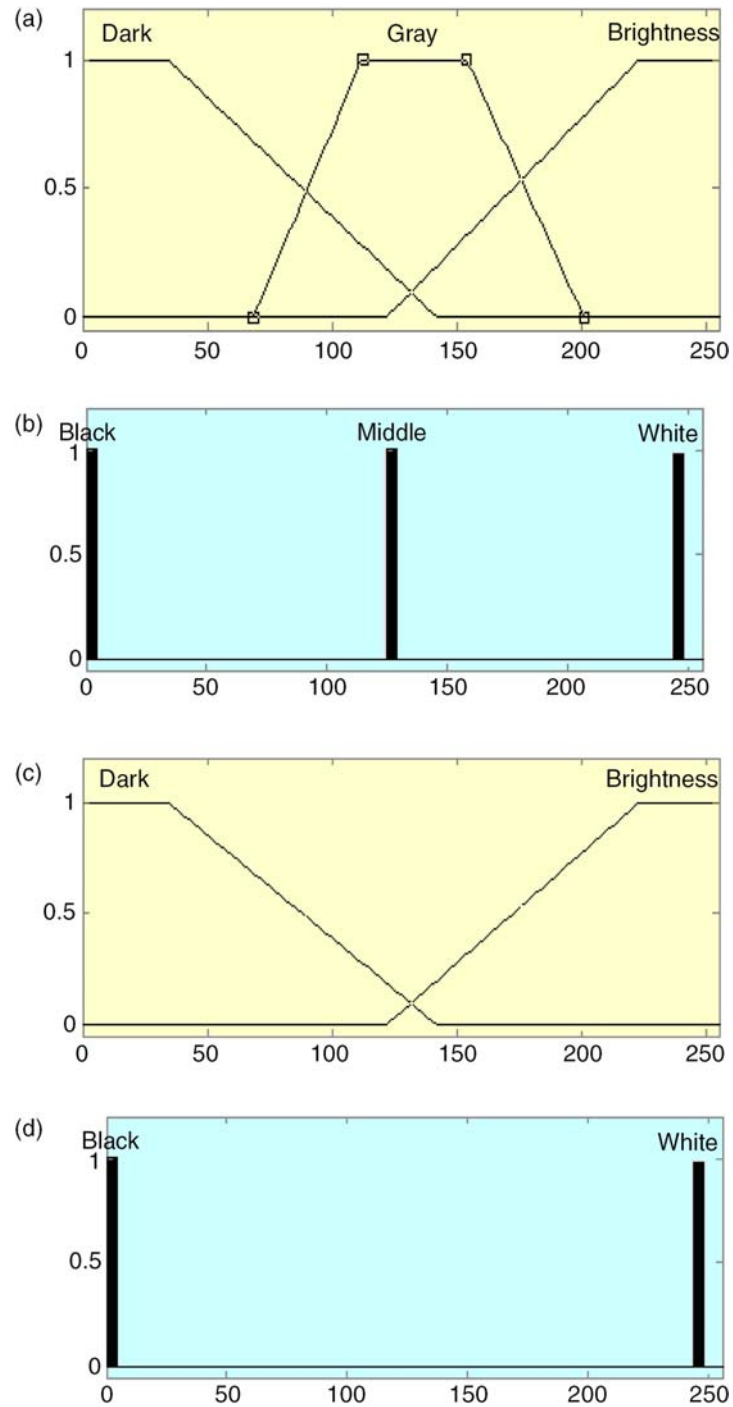


Figure 2. (a) Image fuzzification membership function; (b) Fuzzy inference output function; (c) Image fuzzification membership function; (d) Fuzzy inference output function.

binarization. In this study, fuzzy inference was used to binarize the images in order to filter out noises and highlight image features.

Suppose that the grayscale of pixels  $(x,y)$  in image  $I$  is  $I(x,y)$ , the maximal grayscale in a  $3 \times 3$  image around pixel  $I(x,y)$  will be  $M_{3 \times 3}(x,y)$ , and the grayscale of pixel  $(x,y)$  in output image  $Y$  will be  $Y(x,y)$ . In image fuzzification, the brightness fuzzy function  $\mu_B(x,y)$  represents the fuzzified brightness (brightness), the grayscale fuzzy function  $\mu_G(x,y)$  represents the fuzzified grayscale (gray), and the darkness fuzzy function  $\mu_D(x,y)$  represents the fuzzified darkness (dark), as shown in Figure 2(a).

The number of rules for the fuzzy inference rule base is 3, in which  $y'$  denotes the three fuzzy inference outputs. The fuzzy rule base settings are shown as follows [18–20]:

$$\text{if } I(x, y) \text{ is Brightness then } y'_W \text{ is White} \quad (11)$$

$$\text{if } I(x, y) \text{ is Dark then } y'_B \text{ is Black} \quad (12)$$

$$\text{if } I(x, y) \text{ is Gray then } y'_M \text{ is Middle} \quad (13)$$

After the inferred fuzzy rule is established, the fuzzy output can be obtained. The three fuzzy output functions are shown in Figure 2(b), in which  $y'_W$  denotes the white output, grayscale 255;  $y'_M$  denotes the middle output, grayscale 128; and  $y'_B$  denotes the black output, grayscale 1.

The fuzzy inference rules can be simplified by Eq. (14)–(15), and the fuzzification function is shown in Figure 2(c). As the binarized output is either 0 or 255, only two single-value functions need to be designed to conform to the binarized output, as shown in Figure 2(d):

$$\text{if } I(x, y) \text{ is Brightness then } y'_W \text{ is White} \quad (14)$$

$$\text{if } I(x, y) \text{ is Dark then } y'_B \text{ is Black} \quad (15)$$

When the feature image of the test image is in a high-brightness region, the fuzzy rule of the base setting can binarize the image, as well as accentuate the high-brightness region of the image. Hence, fuzzy inference increases the brightness of the high-brightness pixels and decreases the brightness of the low-brightness pixels. However, when binarized, there will be a significant change of the grayscales in the transitional region between the high brightness and low brightness; namely, the resulting grayscales will have a serrated feature, which can be resolved using an erosion operator. This study adopted an erosion algorithm, which was based on Dubois and Prade's fuzzy set operation of T-Norm [21]. Eq. (16) shows the T-Norm formula:

$$T(a, b) = \frac{a \times b}{\max [a, b, \alpha]} \quad (16)$$

In order to obtain a smoother image, this study added a T-Norm dilation algorithm for binary inference, as follows:

```

α = 0.98
double TNorm(double a, double b)
{
return  $\frac{a \times b}{\max(a, b, \alpha)}$ 
}
While(MeanGray > 4)
{
Newgray =  $\frac{I(x,y)}{256}$ 
for(i = x - 1; i ≤ x + 1; i++){
for(j = x - 1; j ≤ x + 1; j++){
if(i == x && j == y) continue
Newgray = TNorm(Newgray,  $\frac{I(x,y)}{256}$ )
}
}
if Newgray × 255 is Brightness then yw' is White
if Newgray × 255 is Dark then yb' is Black
}

```

The modified fuzzy binarization algorithm maintains the original fuzzy inference and adds the subordinate program TNorm, in order to obtain the T-Norm algorithm of variables a and b. The NewGray variable is resulted from the T-Norm algorithm of the saved  $3 \times 3$  area image of  $I(x,y)$ , and the MeanGray variable is the average grayscale of the saved image. The algorithm is terminated when the average image grayscale is less than 4.

After obtaining the fuzzy output of the fuzzy inference, it must be defuzzified. Height defuzzification was employed for I, as the grayscale of the binarized image was either 255 or 0, and height defuzzification was most suited for a binarization algorithm. Eq. (17) shows the height defuzzification equation:

$$Y(x, y) = \frac{y'_W \times \mu_B(x, y) + y'_M \times \mu_G(x, y) + y'_B \times \mu_D(x, y)}{\mu_B(x, y) + \mu_G(x, y) + \mu_D(x, y)} \quad (17)$$

This study used BPNN to inspect the chemical stains of the back-propagation architecture, which had three layers representing the chemical stain probability; namely, the input layer (seven nodes), the hidden layer (29 nodes), and the output layer (two nodes). The learning algorithm adopted by this study was a back-propagation learning algorithm. In order to determine a chemical stain, this study acquired attributes, such as the area ratio of the light reflection point image, the feature image area ratio, the radian, the feature image geometric distance coefficient of variation (CV), the X-axis and Y-axis projection CVs, and the feature image aspect ratio. Figure 3 shows the differences between a laser reflection point projected onto a chemical stain and onto a non-chemical stain. For the non-chemical stain image, as shown in Figure 3(a),

the projected feature image was close to circular, had a light reflection point brightness, and a halo around the feature image; whereas, the chemical-stained feature image was an irregular geometric figure.

The network inputs in this study employed a number of attributes, such as the light reflection point image area ratio, the feature image area ratio, the radian, the feature image geometric distance CV, the  $X$ -axis and  $Y$ -axis projection CVs, and the feature image aspect ratio.

1. Light reflection point image area ratio:

$$A_{feature} = \frac{A_{LaserSpeckle}}{imageW \times imageH} \quad (18)$$

where,  $A_{feature}$  is the ratio of the feature image area over the light reflection point image area,  $A_{LaserSpeckle}$  is the area of the largest inseparable speckle in the binarized feature image,  $imageW$  is the width of the acquired light reflection point image, and  $imageH$  is the length of the acquired light reflection point image,

2. Feature image radian:

$$e = \frac{4\pi \cdot A_{LaserSpeckle}}{L_{LaserSpeckle}} \quad (19)$$

where,  $A_{LaserSpeckle}$  is the area of the largest inseparable speckle in the binarized feature image,  $L_{LaserSpeckle}$  is the perimeter of the largest inseparable speckle in the binarized feature image, and  $e$  is the calculated radian.

3. Feature image area ratio:

$$A_{ratio} = \frac{A_{Other}}{A_{LaserSpeckle} + A_{Other}} \quad (20)$$

where,  $A_{ratio}$  is the feature image area ratio,  $A_{LaserSpeckle}$  is the area of the largest inseparable speckle in the binarized feature image, and  $A_{Other}$  is the area of the binarized feature image, minus the area of the largest inseparable speckle image.

4. Feature image geometric distance coefficient

$$D_s = \frac{\sqrt{\frac{\sum (D_{xy} - D_{average})^2}{Pixels_{LaserSpeckle}}}}{D_{average}} \quad (21)$$

where,  $D_s$  is the standard deviation of the feature image geometric distance,  $D_{xy}$  is the geometric distance of the feature image pixel from the original,  $D_{average}$  is the geometric mean distance of the feature image, and  $Pixels_{LaserSpeckle}$  is the number of pixels in the binarized feature image, as shown in Figure 3(c).

5. Feature image aspect ratio:

$$Rate = \frac{|Width_{feature} - Height_{feature}|}{Width_{feature} + Height_{feature}} \quad (22)$$

where,  $Rate$  is the feature image aspect ratio,  $Width_{feature}$  is the width of the feature image  $X$ -axis projection, and  $Height_{feature}$  is the width of the feature image  $Y$ -axis projection.

6.  $X$ -axis projection coefficient

$$X_{CRV} = \frac{\sqrt{\sum \frac{X_i - \bar{X}}{Width_{feature}}}}{\bar{X}} \quad (23)$$

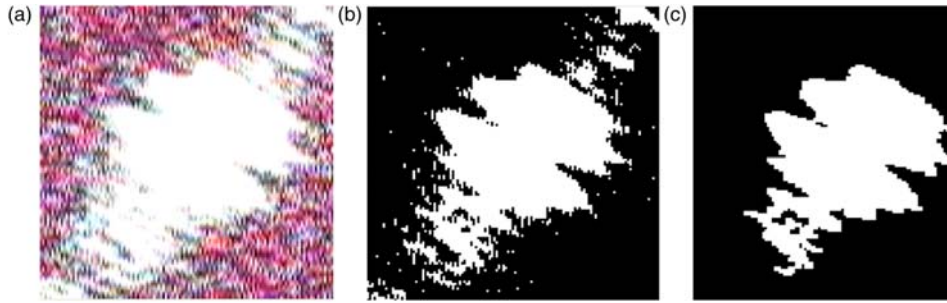


Figure 3. Laser reflection point image acquisition: (a) The acquired laser reflection point feature image; (b) The binarized image; (c) The image of the largest inseparable speckle after binarization.

where,  $X_{CRV}$  is the  $X$ -axis projection coefficient.  $\bar{X}$  is the  $X$ -axis projection mean,  $X_i$  is the projection coordinate on the  $X$ -axis, and  $Width_{feature}$  is the width of the feature image  $X$ -axis projection.

#### 7. $Y$ -axis projection coefficient

$$Y_{CRV} = \frac{\sqrt{\sum \frac{Y_i - \bar{Y}}{Height_{feature}}}}{\bar{Y}} \quad (24)$$

where,  $Y_{CRV}$  is the  $Y$ -axis projection coefficient.  $\bar{Y}$  is the  $Y$ -axis projection mean,  $Y_i$  is the projection coordinate on the  $Y$ -axis, and  $Height_{feature}$  is the width of the feature image  $Y$ -axis projection.

### 3. EXPERIMENTAL RESULTS AND DISCUSSION

In addition to an automatic inspection, the system developed in this study (Figure 4) enabled manual light reflection point image acquisition and back-propagation training. In addition, the parameters could be saved for future usage. The main purpose of this experiment was to obtain laser reflection point images, as seen in Figure 5, in which the image without a stain appears focused and has a quasi-circular shape, while the image with a stained light reflection point shows an irregular geometric figure.

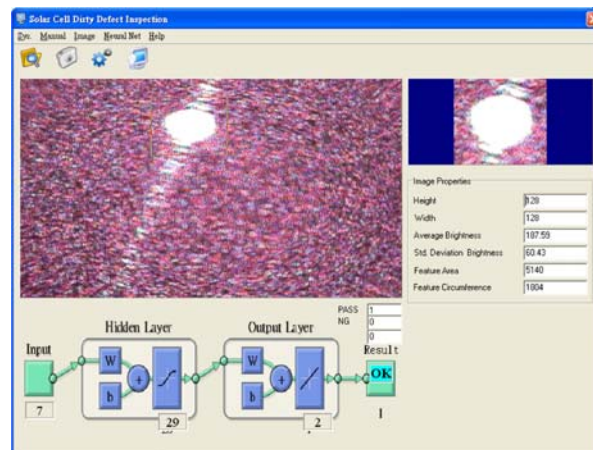


Figure 4. Human-machine interface of the inspection system in this study.

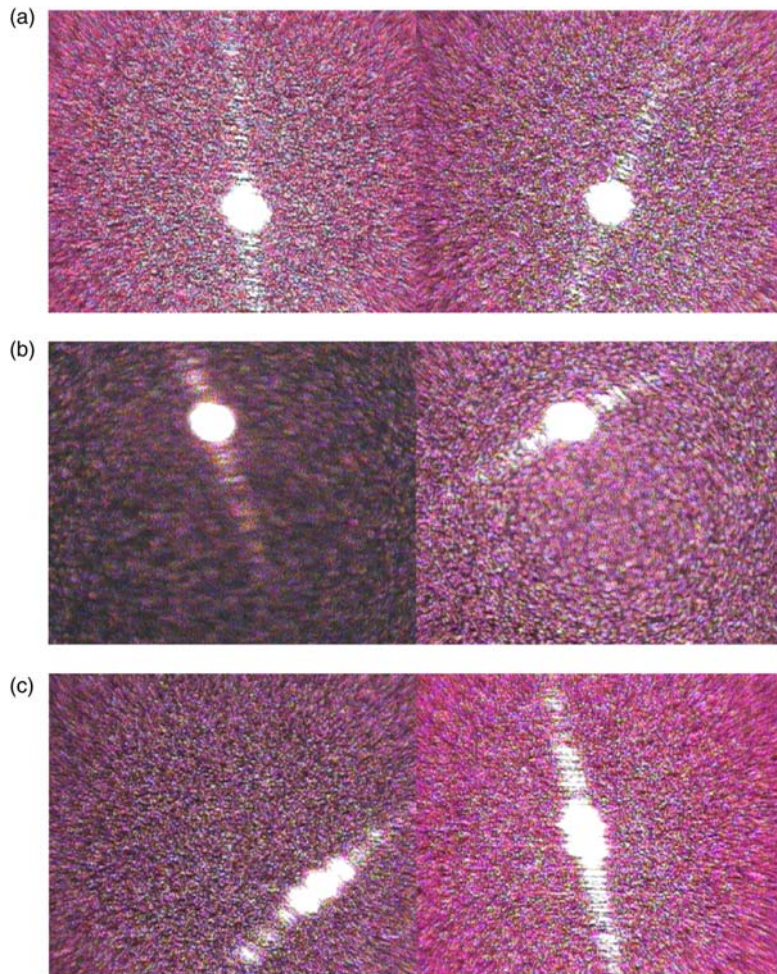


Figure 5. (a) Laser reflection point image (no stain); (b) Laser reflection point image (no stain); (c) Laser reflection point image (with stain).

The images of the laser reflection points were binarized to calculate the eigenvalue as a network input for the learning process. Table 1 lists the network parameters, and Figure 6 shows the errors arising from back-propagation learning. As seen, the back-propagation learning inclined to a convergence, which converged to the expected error after approximately 4000 learning cycles. Figure 7 shows the eigenvalues of the light reflection point image.

Table 1. Back-propagation system.

| Type of neural network                      | Number of network layers | Input Layer    | Hidden Layer  | Output Layer |
|---|--------------------------|----------------|---------------|--------------|
| Back-propagation neural network             | 3                        | 7 neurons      | 29 neurons    | 2 neurons    |
| Sample size of light reflection point image | Learning cycles          | Expected error | Average error |              |
| 36  | 5000                     | 0.01           | 0.009936      |              |

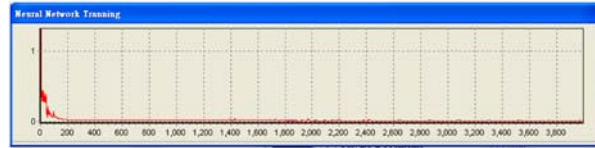


Figure 6. Neural network learning average error.

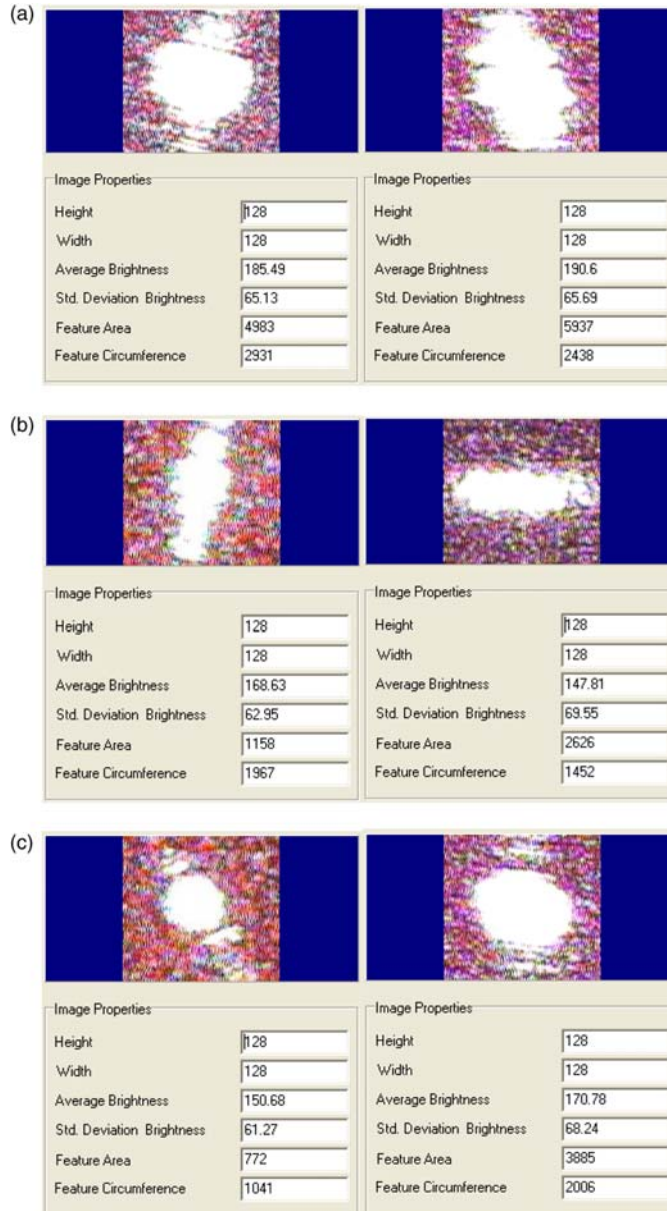


Figure 7. (a) ~ (c) Laser reflection point feature image and eigenvalues.

As seen in Figure 8, the inability or failure to recognize light reflection point feature images was due to the feature images being too small or too bright. As a result, the network determined that the outputs of the feature images were less than 0.6, which led to recognition failure.

Table 2 shows the back-propagation recognition results after the learning experience was completed. In the output layer of the network, the output threshold was 0.6. When the output was greater than 0.6, its eigenvalue would be 1; otherwise, it was 0. According to network recognition, a total of 1096 images were provided for testing light reflection points, in which 747 images had no chemical stains and 340 images had chemical stains, for a recognition rate of 98%.

From the experimental results, the characteristics of the proposed system could be listed as follows:

1. The fuzzy theory was separated from the back-propagation network. The fuzzy neural network architecture proposed by Yu Zhang [14] combines a neural network with fuzzy theory, and then fuzzifies the image's eigenvalues through fuzzy functions and inputs these values into the next layer of the network.
2. The back-propagation method was used to correct the network weights during learning in order to reduce errors.
3. An additional limitation of this study was the fact that the structural details of solar cells are in a random arrangement, and the light reflection point images are also randomly distributed. For different levels of surface roughness, the directions and phases of the scattered laser light will vary with the distribution of the light spots [22]. In other words, violent variations of the surface roughness will influence the accuracy of this system.

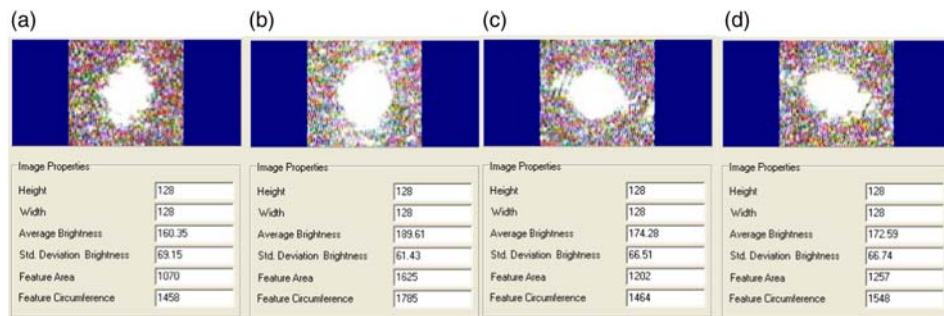


Figure 8. (a) ~ (d) Unrecognizable light reflection point image.

Table 2. Back-propagation recognition results.

| Test samples               | Number of samples without chemical stains | Number of samples with chemical stains |
|----------------------------|---|--|
| 1096                       | 760                                       | 336                                    |
| Recognition result         |   |  |
| Without chemical stains    | 747                                       |  |
| With chemical stains       | 340                                       |  |
| Unrecognizable             | 9   |  |
| Statistic result           |   |  |
| Correct recognition number | 1078                                      |  |
| Recognition rate           | 98%                                       |  |

## 4. CONCLUSIONS

This study combined fuzzy theory with an image-processing algorithm in order to efficiently filter noises from light reflection point images, and it employed inference to fuzzify the results of human decision methods for image processing. The inspection system proposed in this study used a fuzzy theory to process images, and then acquired the image eigenvalues as neural network inputs.

As solar wafer material is fragile, the proposed laser reflection point inspection method could be used to inspect solar wafers without having to make contact. Future studies could incorporate a computer-integrated manufacturing technique in order to develop a more comprehensive manufacturing automation process, which would increase the capacity, quality, and yield.

## ACKNOWLEDGEMENTS

This work was sponsored by the National Science Council under grant number NSC 101-2221-E-035 -039 -MY2 and the help of Mosel Vitelic Inc.

## REFERENCES

- [1] Green, M. A. (March 2003). Crystalline and thin-film silicon solar cells: state of the art and future potential. *Solar Energy*, 74(3), 181–192.
- [2] Lee, G. H., Rhee, C. K., & Lim, K. S. (February 2006). A study on the fabrication of polycrystalline Si wafer by direct casting for solar cell substrate. *Solar Energy*, 80(2), 220–225.
- [3] Schmich, E., Schillinger, N., & Reber, S. (September 2007). Silicon CVD deposition for low cost applications in photovoltaics. *Surface and Coatings Technology*, 201(22–23), 9325–9329.
- [4] Schirone, L., Sotgiu, G., & Califano, F. P. (April 1997). Chemically etched porous silicon as an anti-reflection coating for high efficiency solar cells. *Thin Solid Films*, 297(1–2), 296–298.
- [5] Barrio, R., Maffiotte, C., Gandía, J. J., & Cárabe, J. (June 2006). Surface characterisation of wafers for silicon-heterojunction solar cells. *Journal of Non-Crystalline Solids*, 352(9–20), 945–949.
- [6] Bau, S., Rentsch, J., Huljić, D. M., Reber, S., Hurre, A., & Willeke, G. (May 2003). Application of screen printing processes for epitaxial silicon thin-film solar cells. *3rd World Conference on Photovoltaic Energy Conversion*, 2, 1356–1359.
- [7] Istratov, A. A., Hieslmair, H., Vyvenko, O. F., Weber, E. R., & Schindler, R. (April 2002). Defect recognition and impurity detection techniques in crystalline silicon for solar cells. *Solar Energy Materials and Solar Cells*, 72(1–4), 441–451.
- [8] Arafune, K., Sasaki, T., Wakabayashi, F., Terada, Y., Ohshita, Y., & Yamaguchi, M. (April 2006). Study on defects and impurities in cast-grown polycrystalline silicon substrates for solar cells. *Physica B: Condensed Matter*, 376–377, 236–239.
- [9] Daami, A., Zerrai, A., Marchand, J. J., Poortmans, J., & Brémond, G. (February 2001). Electrical defect study in thin-film SiGe/Si solar cells. *Materials Science in Semiconductor Processing*, 4(1–3), 331–334.
- [10] Belyaev, A., Polupan, O., Ostapenko, S., Hess, D., & Kalejs, J. P. (January 2006). Resonance ultrasonic vibration diagnostics of elastic stress in full-size silicon wafers. *Semiconductor Science and Technology*, 21, 254–260.
- [11] Li, Q., Wang, W., Ma, C., & Zhu, Z. (September 2010). Detection of physical defects in solar cells by hyperspectral imaging technology. *Optics and Laser Technology*, 42(6), 1010–1013.
- [12] Hilmersson, C., Hess, D. P., Dallas, W., & Ostapenko, S. (August 2008). Crack detection in single-crystalline silicon wafers using impact testing. *Applied Acoustics*, 69(8), 755–760.
- [13] Tsai, D. M., Chang, C. C., & Chao, S. M. (March 2010). Micro-crack inspection in heterogeneously textured solar wafers using anisotropic diffusion. *Image and Vision Computing*, 28(3), 491–501.
- [14] Zhang, Y., & Zhang, J. (October 2005). A Fuzzy neural network approach for quantitative evaluation of mura in TFT-LCD. *2005 International Conference on Neural Networks and Brain*, 1(13–15), 424–427.
- [15] LV, Y., WU, M., Lei, Q., & Nie, Z. Y. (2011). Soft sensor based on a pso-bp neural network for a titanium billet furnace-temperature. *Intelligent Automation and Soft Computing*, 17(8), 1207–1216.
- [16] Pan, W. J., Jiang, C. Y., Tang, Y. J., & Yang, S. X. (2011). Tobacco dry weight estimation based on artificial neural network. *Intelligent Automation and Soft Computing*, 17(7), 997–1007.
- [17] Egmont-Petersen, M., de Ridder, D., & Handels, H. (2002). Image processing with neural networks—a review. *Pattern Recognition*, 35(10), 2279–2301.
- [18] Tizhoosh, H. R. (1998). Fuzzy image processing: potentials and state of the art. *5th International Conference on Soft Computing*, Iizhka, Japan 321–324.
- [19] Mendel, J. M. (1995). Fuzzy logic systems for engineering: a tutorial. *Proceedings of the IEEE*, 83(3), 345–377.

- [20] Chen, S. J. (2011). Fuzzy information retrieval based on a new similarity measure of generalized fuzzy numbers. *Intelligent Automation and Soft Computing*, 17(4), 465–474.
- [21] Franke, K., Koppen, M., & Nickolay, B. (2000). Fuzzy image processing by using dubois and prade fuzzy norms. *15th International Conference on Pattern Recognition*, 518–521.
- [22] Lin, C. S., Haun, C. M., Hsien, F. S., Yeh, M. S., Chao, C. S., & Chen, R. (2011). Application of laser speckle technology in solar wafer roughness inspection system. *Indian Journal Of Pure & Applied Physics*, 49(8), 523–530.

## NOTES ON CONTRIBUTORS



**Chern-Sheng Lin** received his B.S. degree from National Cheng Kung University, Taiwan, in 1982, M.S. degree in Mechanical Engineering from the National Taiwan University, in 1987, and Ph.D. degree in Optical Science from the National Central University, in 1994. Since 1995 he has been with the Department of Automatic Control Engineering at Feng Chia University in Taiwan where he is now a Distinguished Professor. His current research interests include pattern recognition, image processing, and human-machine interface design.



**Chih-Wei Lin** received his B.S. degree in Department of Automatic Control Engineering, Feng Chia University, in 2007. He is now an Engineer of electronic control systems for AUO Inc.



**Shih-Wei Yang** received his B.S. degree from Department of Electrical Engineering, National University of Kaohsiung, Taiwan, in 2010, and M.S. degree from Department of Electrical Engineering, Feng Chia University, Taiwan, in 2012. He is now a doctoral student at Institute of Electrical Control Engineering, National Chiao Tung University, Taiwan. His current research interests include Automatic Optical Inspection (AOI) system design, machine vision technology, and automation.



**Shir-Kuan Lin** received his B.S. degree from the Department of Aeronautics and Astronautics, National Cheng Kung University, Taiwan, in 1979; M.S. degree from the Department of Power Mechanical Engineering, National Tsing Hua University, Taiwan, in 1983; and Ph.D. degree in the Department of Mechanical Engineering, University of Erlangen-Nurnberg, Germany, in 1988. He is now a professor at the Institute of Electrical Control Engineering, National Chiao Tung University, Taiwan. His current research interests include circuit theory, adaptive control systems, and microcomputer.



**Chuang-Chien Chiu** received his B.S. degree in Electrical Engineering from Feng Chia University, Taiwan, R.O.C. in 1986. He received his M.S. degree in 1991 and Ph.D. degree in 1993, both in Electrical Engineering, from Michigan State University, East Lansing, MI. Since August 1993, he has been with the Department of Automatic Control Engineering, Feng Chia University, Taiwan, R.O.C., where he is currently a Professor. He served as the Chairman of the Department of Automatic Control Engineering of Feng Chia University from 1998 to 2000. He also served as Dean of the College of Information and Electrical Engineering from 2001 to 2008, and the director of the Graduate Institute of Electrical and Communications Engineering of Feng Chia University from 2001 to 2007. He was a visiting scholar of the University of Wisconsin at Madison from 2008 to 2009. His current research interests include ambulatory monitoring with wearable technology (smart shirt), biomedical signal processing and neural networks, with particular emphasis on physiological signal analysis for autonomic nervous system, speech analysis, image processing, and developing real-time medical system for tongue diagnosis and objective auscultation in traditional Chinese medicine. Dr. Chiu is a member of Phi Tau Phi and Phi Beta Delta. He is also a member of the IEEE Engineering in Medicine and Biology Society.